Correspondence to:
S. Khaksarighiri, J. Guo, and R. F. Wimmer-Schweingruber,
khaksari@physik.uni-kiel.de;
jnguo@ustc.edu.cn;
wimmer@physik.uni-kiel.de

The Zenith-Angle Dependence of the Downward Radiation Dose Rate on the Martian Surface: Modeling Versus MSL/RAD Measurement

Salman Khaksarighiri[1] , **Jingnan Guo[2,3]** , **Robert F. Wimmer-Schweingruber[1]** , **Sven Löffler[1]**, **Bent Ehresmann[4]** , **Daniel Matthiä[5]** , **Donald M. Hassler[4]** , **Cary Zeitlin[6]** , and **Thomas Berger[5]**

[1]Institute of Experimental and Applied Physics, Christian-Albrechts-University, Kiel, Germany, [2]Deep Space Exploration Laboratory/School of Earth and Space Sciences, University of Science and Technology of China, Hefei, PR China, [3]CAS Center for Excellence in Comparative Planetology, USTC, Hefei, PR China, [4]Solar System Science and Exploration Division, Southwest Research Institute, Boulder, CO, USA, [5]German Aerospace Center (DLR), Institute of Aerospace Medicine, Cologne, Germany, [6]Leidos Corporation, Houston, TX, USA

Abstract The Radiation Assessment Detector (RAD) on board the Mars Science Laboratory's Curiosity rover has been monitoring the surface radiation environment on Mars for just over 10 years. It has been found by Wimmer-Schweingruber et al. (2015, https://doi.org/10.1002/2015gl066664) that within the narrow view cone of RAD, the directionality of the radiation field is close to but not completely isotropic. In order to better understand the directionality of the surface radiation over a wide range of zenith angles (θ), we perform a three-dimensional Geant4 Monte Carlo simulation to derive the θ-dependence of the surface dose rate. The results show that galactic cosmic ray protons, coming in at $\theta \sim 74°$ make the greatest contribution to the surface dose. For helium ions, this angle is at around 46°. This is a consequence of the increasing column depth at larger zenith angles and the complex interplay of the destruction of primary and the creation of secondary particles as the primary cosmic ray interacts with the Martian atmosphere. We also compared the simulated results with the RAD measurements and found a reasonable agreement. Our results are important for future human exploration of Mars, for instance, to estimate the effectiveness of radiation shielding of a given geometry or for optimizing the radiation shielding design of a Martian habitat.

Plain Language Summary Space agencies and private companies are working to place humans on the surface of Mars. Astronauts would be exposed to a different and considerably harsher radiation environment on Mars than humans are on Earth. Space radiation is largely determined by galactic cosmic rays, which have sufficient energy to reach the Martian surface. Thus, a better understanding of the radiation on the surface of Mars is needed. The shielding provided by the atmosphere increases with the zenith angle, and it also causes an increase in the creation of secondary particles. To better understand this, we perform a Geant4 Monte Carlo simulation to derive the dependence of the surface dose rate on the zenith angle θ. The results show that the radiation dose on the surface of Mars depends on the incoming angle of the primary radiation. Moreover, the radiation dose rate is significantly modulated by solar activity, and the Mars surface dose rate differs by about 50% between solar maximum and minimum periods. We validate our simulation by comparing the dose measured by the Mars Science Laboratory Radiation Assessment Detector and find good agreement.

1. Motivation and Introduction

Future expeditions into interplanetary space, and in particular to the Moon and Mars, will expose astronauts to much higher levels of cosmic radiation compared to the current low-Earth orbit (LEO) missions due to the strong shielding against interplanetary radiation provided by the Earth's magnetic field that attenuates the major effects of space radiation exposures for current LEO missions. Deep space is dominated by two major sources of energetic particle radiation: background Galactic Cosmic Rays (GCRs) and sporadic, but highly variable in intensity Solar Energetic Particles (SEPs). Protons and helium ions comprise about 87% and 12% of GCR nuclei with traces of heavier nuclei such as carbon, nitrogen, oxygen, and iron (Simpson, 1983). SEPs are dominated by protons and electrons, which are accelerated during sporadic solar eruptions and released into interplanetary space.
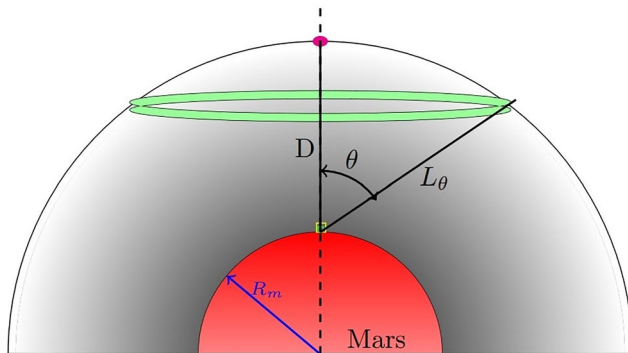
Figure 1. Schematic view of a full-size spherical Mars as a substrate; and is a representation of the real-world system. The red hemisphere represents a hemisphere of Mars. The position of the Radiation Assessment Detector is indicated by a green square with a yellow border. The green ring is an example of ring sources, and the magenta point represents the source with θ equal to 0°. More information can be found in the text.

Exposure to deep space radiation can lead to health risks such as acute and long-term effects for astronauts (Barcellos-Hoff et al., 2015; Cucinotta & Durante, 2006). SEPs can deliver a very high level of radiation over a short time to the human body and may cause acute radiation effects, such as nausea and vomiting or death in the worst case. Long-term exposure to GCRs does not cause immediate health effects but can increase the risk of cancer over a lifetime and also cataracts and central nervous system decrements (Cucinotta et al., 2014; Kennedy, 2014; Khaksarighiri et al., 2021). Thus, a better understanding of the radiation environment for space missions is necessary and fundamental for the safety of astronauts.

When GCRs and SEPs arrive at Mars, they can interact with the Martian atmosphere and lose energy via ionization processes, and they can also create secondary particles via spallation and fragmentation processes. With sufficient energy, they can arrive at the Martian surface and further penetrate the subsurface and produce secondary particles in both the atmosphere and soil. As a result, the radiation environment on the Martian surface is different from that in deep space (Guo, Zeitlin, et al., 2021; Wilson et al., 2004). The Radiation Assessment Detector (RAD, Hassler et al., 2012) on board the Mars Science Laboratory's (MSL) Curiosity rover has been monitoring the surface radiation environment on Mars for just over 10 years since its landing in 2012 August. The shielding effect of Mars's atmosphere has been shown to be more important than the creation of secondary radiation (Guo et al., 2017; Rafkin et al., 2014).

Radiation in deep space is nearly isotropic most of the time, that is, it comes from the full 4π solid angle. On the Martian surface, the planet itself provides excellent shielding against energetic particle radiation that would come from the bottom half of the full solid angle. There is, however, a small portion of the radiation that is directed upward. These secondary, upward-directed "albedo" particles are generated in the soil as by-products of the interaction of the GCR with the soil. Guo, Khaksarighiri, et al. (2021) estimated that the albedo radiation, measured as an absorbed dose by RAD, on flat terrain is about 19% of the total surface dose, that is, most of the radiation detected on the Martian surface is due to downward-directed particles.

While the primary GCRs are nearly isotropic in deep space, their angular distribution is modified as they travel through the Martian atmosphere to reach the surface. Particles coming through the atmosphere from the horizon need to pass through a much larger atmospheric column depth than particles coming from the vertical direction. The atmospheric column depth that a particle must traverse to reach the surface increases with zenith angle θ, which represents the angle from the surface normal as shown in Figure 1.

At $\theta = 0$°, the atmospheric column depth is about ~21 g/cm^2 at Curiosity's location in the Gale Crater. For comparison, at a zenith angle of ~90° the corresponding column depth is ~400 g/cm^2.

As Curiosity moves across the surface, its inclination with respect to the surface of an idealized, spherical Mars changes due to local topography. Wimmer-Schweingruber et al. (2015) used these variations to study the radiation shielding effect of the atmosphere and found that the radiation field is close to isotropic with a slight increase of shielding toward larger zenith angles. That study was limited to a maximum rover tilt angle of $\lesssim 15$°.

In order to better understand the directionality of the surface radiation over a wider range of zenith angles (θ), we perform a three-dimensional Geant4 (GEometry And Tracking, Agostinelli et al., 2003, 2006, 2016) Monte Carlo simulation to derive the θ-dependence of the surface dose rate. Specifically, we model the interaction of the incoming GCRs with the Martian atmosphere and also with the RAD detector to derive the surface radiation field across a large range of zenith angles. We thus investigate the zenith-angle dependence of dose (energy per mass) deposited in RAD.

In this paper, we first explain our model, especially the setup of the Martian environment and the input particle sources in Section 2. The modeled results and their zenith angle-dependence are presented in Section 3, including also the model prediction of RAD measurements. Finally, we validate our model in Section 3.3, using the dose measured by RAD within two telescope view cones to compare with our modeled results.
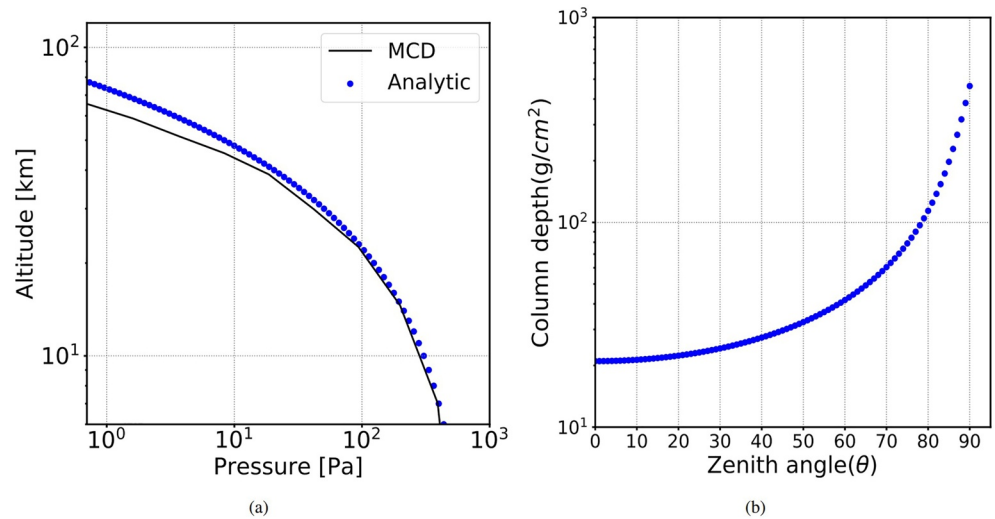
Figure 2. (a): Comparison of the pressure on the surface of Mars versus altitude based on the analytical model and the data obtained from the Mars Climate Database (b): CO_2 column depth for different zenith angles on the surface of Mars.

2. Model Description and Implementation

In order to build our geometry in Geant4, we first need to calculate the atmospheric column depth as a function of the zenith angle on the surface of Mars. Figure 1 has been used for this purpose, which illustrates a full-size spherical Mars as a substrate; and is a representation of the real-world system.

Considering Figure 1 we can derive the following equation:

$$(R_m + D)^2 = R_m^2 + L_\theta^2 + 2R_m L_\theta \cos(\theta). \tag{1}$$

Here R_m is Mars's radius, L_θ is the effective scale height which depends on the zenith angle θ, and D is the distance between RAD and the magenta point. The atmospheric column depth (σ) and its dependency on the zenith angle (θ) for each ring can be derived as follows:

$$L_\theta = -R_m \cos(\theta) + \sqrt{R_m^2 \cos(\theta)^2 + D^2 + 2R_m D}. \tag{2}$$

We approximate the atmospheric density with the well-known barometric expression and find

$$\sigma = \int \rho_0 e^{-h/H} dh \tag{3}$$

where H is the scale height, ρ_0 is the atmospheric density on the surface of Mars, h represents the atmospheric height, and σ is the integrated atmospheric column depth in the vertical direction $\theta = 0°$, which is set to 21 g/cm^2 in this model and calculate the D, which is the distance between the RAD and magenta point. As the pathlength through each thin spherical shell of roughly constant density along the two paths at θ and $0°$ is in the same ratio as L_0 and D, we can modify Equation 3 as follows:

$$\sigma = \rho_0 \times L_\theta. \tag{4}$$

where σ represents the CO_2 column depth (g/cm^2) in different zenith angles.

With this model, we calculate the CO_2 column depth in different zenith angles on the surface of Mars shown in Figure 2b and used these data to build the Mars surface geometry in our model as different hemispheres in Figure 3, each hemisphere belong to a specific column depth correspond to the zenith angle.

Mars Climate Database (MCD, Millour et al., 2015, http://www-mars.lmd.jussieu.fr/) is a database containing Martian meteorological variables developed using various Martian atmospheric models and validated against available observational data (Millour et al., 2015). We compared the pressure at a certain height versus
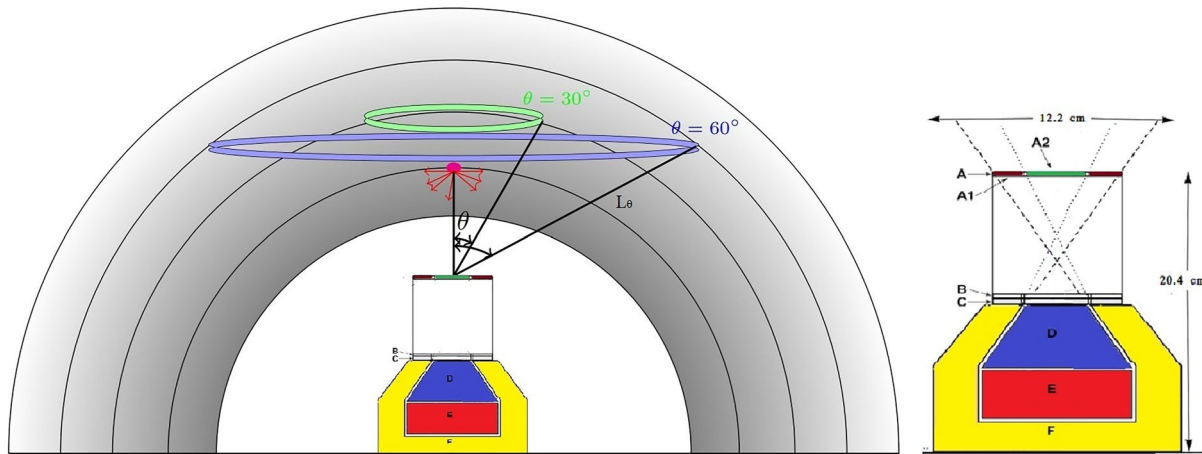
Figure 3. Schematic views of the zenith-angle (θ) dependence of the Mars atmospheric setup (left) and the Radiation Assessment Detector sensor head (right, adapted from Hassler et al. (2012)). The green and blue rings are example ring sources with θ being 30° and 60°, respectively, and the magenta point represents the source with θ equal to 0°. More information can be found in the text.

atmospheric altitude (between 0 and 95 km) based on the above analytical model with the data obtained from the MCD, as shown in Figure 2a. The vertical atmospheric distribution based on our model agrees well with MCD with less than 1% difference for altitudes lower than 35 km on the Martian surface, but the difference reaches 13% at higher altitudes because of the complexity of the MCD model compared to our simple model of the Martian surface. The right panel of Figure 2 shows the atmospheric column depth σ as a function of zenith angle θ as obtained from our model (Equation 4).

We include the RAD detector in our model, as shown in Figure 3 to allow the comparison of simulations with measurements as presented in Section 3.3. The Martian atmosphere is modeled as pure CO_2 because it makes up about 95% of the Martian atmosphere. The vertical ($\theta = 0°$) atmospheric column depth is about 21 g/cm^2 when the surface pressure is about 800 Pa, which is the average value measured by MSL at Gale Crater (REMS, Gómez-Elvira et al., 2012), and column depth increases with increasing θ toward the horizon as shown in the right-hand panel of Figure 2.

2.1. Geant4 Toolkit

We used version 10.4 of the Geant4 (GEometry And Tracking, Agostinelli et al., 2003, 2006, 2016) three-dimensional Monte Carlo particle transport tool with the QGSP BERT physics list. The QGSP BERT physics list applies the quark-gluon string model for high energy particles (≥ 20 GeV) and the Bertini cascade model in the middle and low energy range. In the model, the excited nuclei that are generated by high energy interactions are passed to the Precompound model which is used to describe the de-excitation process. In terms of modeling the Martian radiation environment, it has been found that different physics lists can affect the generation of secondary particles, especially those produced via spallation processes (Guo et al., 2019). However, the surface absorbed dose normally agrees within ~5% for different physics lists (Matthiä et al., 2016).

2.2. Model Description

As discussed above, the interaction of GCRs with a planetary atmosphere leads to a change in the isotropic nature of the radiation field, which results in a higher directional flux of primary particles from the zenith than from the horizon. This can be understood due to the interaction of primary particles with the atmosphere, which has a much smaller column depth in the zenith direction than toward the horizon. Our model is set up in order to quantify the above effect and to determine the surface dose rate arriving from different zenith angles.

The RAD sensor head shown in the right panel of Figure 3 is placed on the Martian surface in our model and consists of three silicon detectors (A, B, and C), a cesium iodide scintillator D, and a plastic scintillator E (Hassler et al., 2012). Absorbed dose values are simultaneously recorded and also modeled in detectors B and E with the
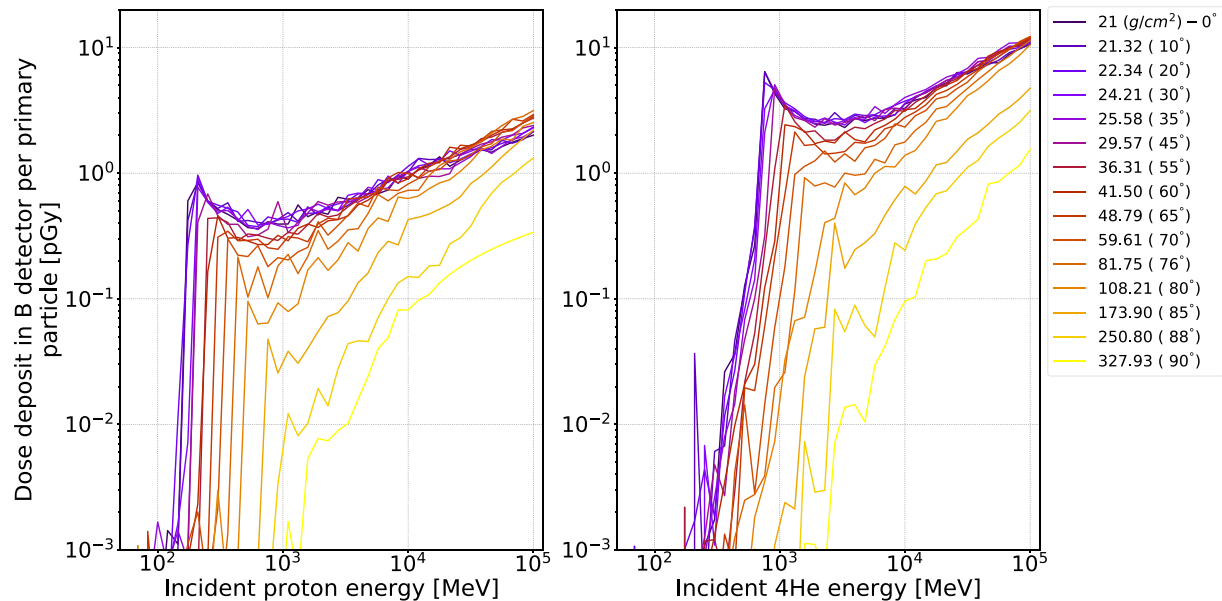
Figure 4. Simulated dose deposit in the Radiation Assessment Detector B detector as a function of the primary particle energy at various zenith angles with different column depths (represented by different line colors) for protons (left) and ^{4}He ions (right).

masses of 1.3×10^{-4} kg and 34.9×10^{-3} kg, respectively. Both scintillators are surrounded by a plastic anticoincidence scintillator (F). The modeled geometry corresponds exactly to the RAD geometry, which is a small packed instrument with a total mass of 1.5 kg. As simulating dose to RAD embedded in a planet-scale illuminated volume of atmosphere would take forever to build up statistics, we have compressed the atmospheric representation starting from 25 cm on top of the RAD and more layers with different densities of CO_2 will be added for larger zenith angles and reach to 125 cm for the last layer in 400 g/cm^2 of CO_2. σ calculated in Equation 4 represents the column depth of the atmosphere, which increases with the zenith angle from vertical to horizontal directions, as shown in Figure 2b. The gray scale represents the Mars atmosphere which is set to be 100% CO_2 in this model. The green and blue rings are example ring sources with θ being 30° and 60° placed in various layers with corresponding column depth of atmosphere, respectively. The magenta point represents the source with θ equal to 0° corresponding to 21 g/cm^2 of CO_2, placed on top of the first layer of CO_2 with 30 cm of radius. The RAD itself has been placed in a high vacuum hemisphere, which means all the primary and secondary particles will follow their direction, after passing through the CO_2 layers.

High-energy particles at the top of Mars' atmosphere do not necessarily follow the black line labeled L_θ in Figure 3, but are scattered, they lose energy, and—if energetic enough—may create secondary particles or even a shower of secondary particles. To account for this, we placed our primary particle sources along spherical segments of constant zenith angle, as indicated by the green and blue rings at 30° ± 1° and 60° ± 1° in Figure 3. From the inner surface of each ring, particles were launched with an inward cosine directional distribution with a power-law index of −1 to result in an isotropic homogeneous field inside the hemisphere as shown with red arrows for the magenta source. The modeled energies of primary protons and ^{4}He ions were distributed from 1 MeV to 100 GeV in 62 logarithmically spaced bins to simplify the rebinning and convolutions with different primary GCR spectra, as explained later. For each such spherical segment, a total of 6.2×10^7 particles of the two-particle types were simulated, that is, 10^6 particles per energy bin.

3. Simulation Results and Comparison With Measurements

The results of the total dose (absorbed by the RAD B 300-μm silicon detector) per particle versus the incoming energy of particles from 1 MeV to 100 GeV for different zenith angles (or column depths) are shown in Figure 4 with left and right panels for protons and ^{4}He ions, respectively. The simulations are performed for detector B without regard to coincidence or anticoincidence, and then the dose rates are restricted to the A1B and A2B acceptance cones for comparison with observations that will be explained in more detail in Section 3.3.

As shown in Figure 4, there is a sharp increase in the surface dose contribution from protons at 164 MeV/nuc for 0° zenith angle. This "cutoff" energy is equivalent to the energy required for particles to penetrate 21 g/cm^2 of carbon dioxide, which is 164 MeV for protons and 630 MeV for ^{4}He ions and defined as 10% of the peak dose at 0° zenith angle. The small contributions to the surface dose below this primary energy are mainly from proton-generated secondaries such as electrons, gammas, and neutrons. Figure 4 also shows that this cutoff energy depends on the zenith angle (which is color-coded in this figure), and that larger zenith angles have a larger cutoff energy because of the larger column depth that particles need to penetrate. As expected, the dose from the lowest energy particles is seen for the thinnest column depth whereas the thickest column depth results in a lower energy deposit.

The simulation results also show that at energies lower than ∼1 GeV/nuc, the dose decreases as the primary energy increases as is to be expected from the Bethe-Bloch approximation (Bethe, 1930; Bloch, 1933). But, at energies above the relativistic minimum of around 1 GeV/nucleon, the electromagnetic ionization dose per unit pathlength departs from the Bethe-Bloch approximation and starts to increase with energy; this, together with the generation of secondary particles, particle fragmentation, and spallation interactions in the atmosphere lead to a rise in dose per primary particle toward high energies.

Note that the total dose in our model comprises all primary particles and secondary particles generated by primaries interacting with the atmosphere which are detected by the RAD within a small zenith angle range (from $\theta - 1°$ to $\theta + 1°$) of the primaries.

This assumption is more reliable when the atmosphere is thin, as in the case of Mars, and a small number of secondaries are generated.

3.1. Procedure of the Model Application

Figure 4 shows the dose deposited in the RAD B detector by an individual primary particle versus its primary energy. In this section, we show how to weight this result with various GCR input spectra to compute the dose rate measured by the RAD B detector. Figure 5 gives a visual summary of the procedure and shows the results for the example of primary GCR protons. The procedure for ^{4}He ions (right-hand panel of Figure 4) is the same, but not shown here. The proton dose distributions for different zenith angles in the B detector, that is, Figure 4a shows the dose deposit in the B detector per primary particles and is multiplied by the area and solid angle of primary rings in each zenith angle and gives us the dose deposit per primary fluence [μGy]/[particles/cm^2 sr] shown in Figure 5a.

Various input spectra of the GCR proton flux in deep space are shown in Figure 5b. These primary GCR spectra are predicted by the Badhwar O'Neill 2014 model (BON, O'Neill et al., 2015) for different solar modulation potentials as indicated in the legend.

We then multiplied a dose-deposit function of a certain θ value in Figure 5a with a GCR input spectrum from Figure 5b by first multiplying the functions in Figure 5a by the widths of the energy bins used in the simulation to have units of [μGy]/[particles/cm^2 sr MeV] and then multiplying the values of this normalized function with the differential flux in each corresponding energy-bin. Taking the GCR spectrum with Φ of 400 MV as an example, we obtain the dose rate as a function of energy as shown in panel (c) for different inclination angles, θ. For each θ, the total dose summed over all energy bins would be the expected radiation in RAD B from that zenith angle. Note that the total dose is induced by primary GCR protons and also the secondaries generated by primary protons in the atmosphere. The same procedure is used to derive GCR ^{4}He induced dose for each θ angle and also for different solar modulation conditions.

Mathematically, the procedure described above can be summarized as given in Equation 5:

$$\dot{D} = \left\{ \frac{D}{f} \right\} \times F, \tag{5}$$

where D (μGy) is the dose-deposit function of a certain θ value from the Geant4 simulation, f is the fluence of the source used in the simulation given as the number of particles per cm^2 sr MeV, and F represents the differential flux of GCRs given as the number of particles per cm^2 sr MeV and sec, which finally gives us $\dot{D}$, that is, the dose rate per energy bin in the B detector of RAD for the surface of Mars in each zenith angle.
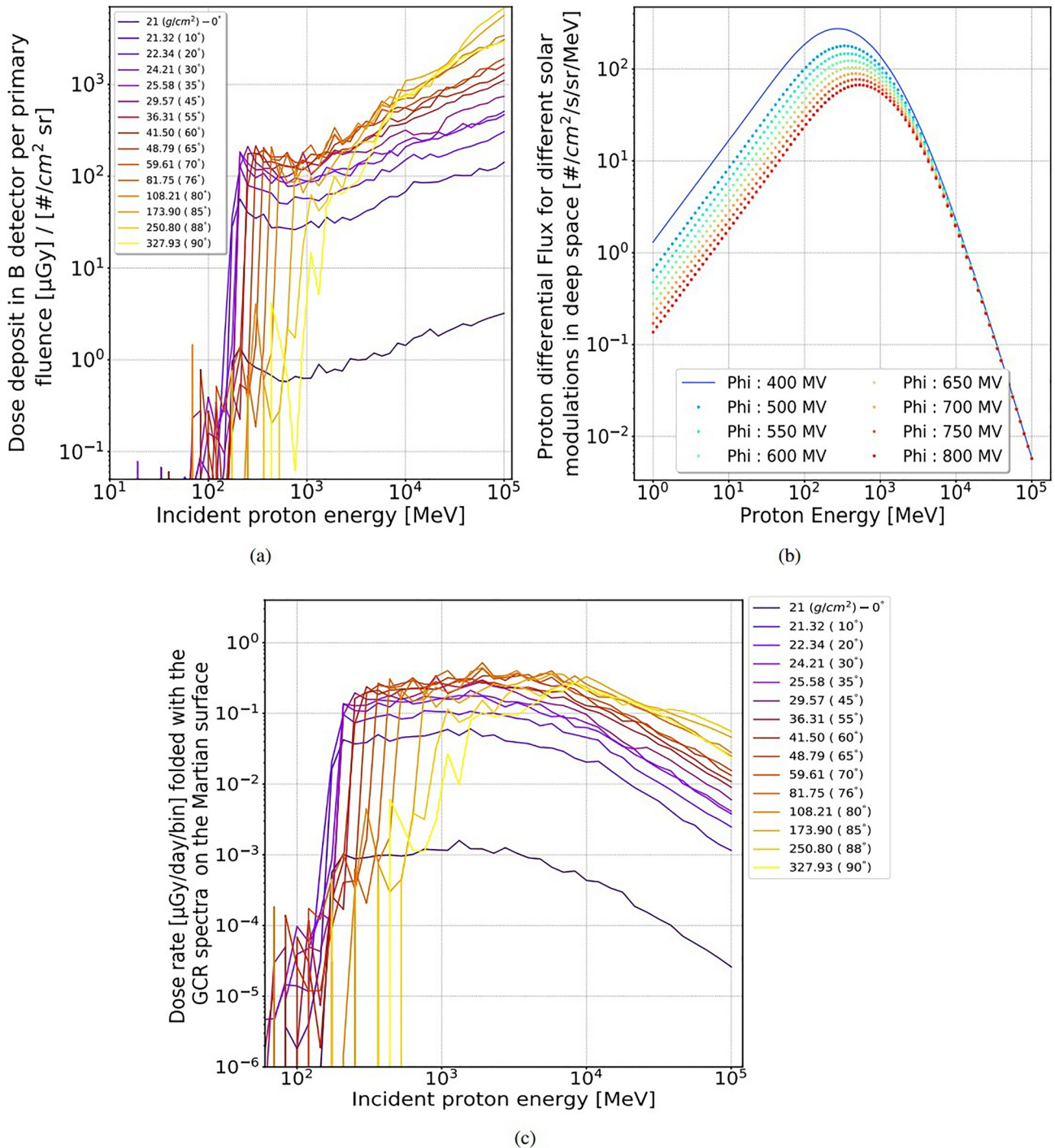
Figure 5. Multiplying the precalculated dose functions in Figure 4 with input galactic cosmic ray (GCR) spectra to calculate the Martian surface dose rate as measured in the Radiation Assessment Detector (RAD) B detector. (a): Proton dose functions in the RAD B detector for different zenith angles (normalized to the [particles/cm² sr]). (b): Energy- and time-differential flux of GCR protons for different solar modulation potentials Φ (MV). (c): Multiplication results of the dose-response functions of the panel (a) with the 400 MV primary GCR spectrum in panel (b) in each corresponding energy bin. More details can be found in Section 3.1.

3.2. Modeled Zenith-Angle Dependence of Dose in RAD-B on Mars

After integrating the dose rate in Figure 5c over energy, we obtain the expected RAD-B dose rate from each θ direction. Results for different solar modulation potentials are easily derived with the same procedure but using a different input spectrum from panel b in Figure 5. Figure 6 shows the thus predicted dose rate in the RAD-B
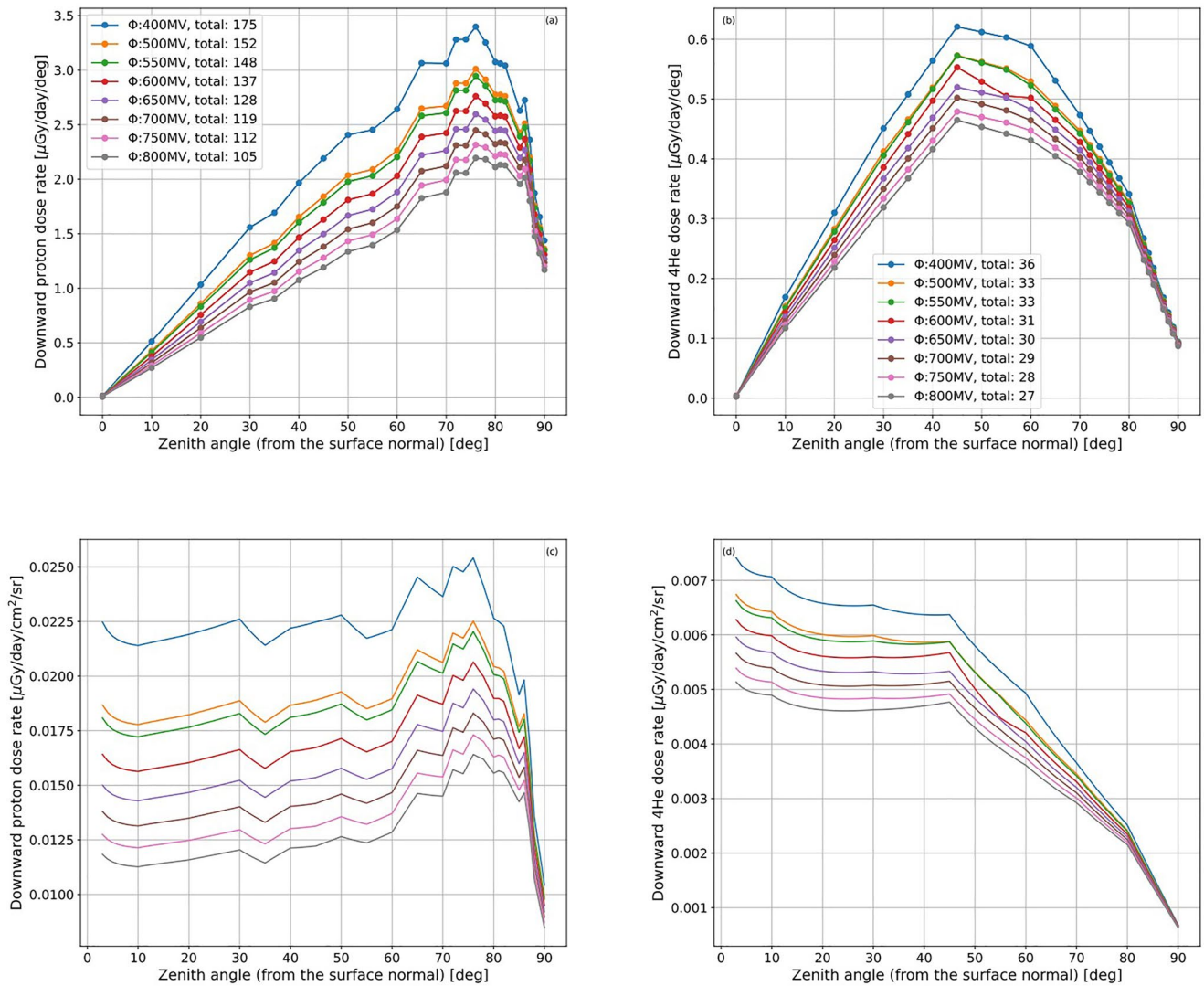
Figure 6. Dependence of modeled dose rate in the Radiation Assessment Detector B detector on zenith angle (θ) for (a)/(c) primary galactic cosmic ray (GCR) protons and (b)/(d) ^{4}He ions. Different primary GCR spectra are considered under different solar modulation potentials Φ shown in different colors. (a, b) show the dose rate per degree of θ; (c, d) show the dose rate scaled to per solid angle. Total dose rate [μGy/day] integrated over θ is also given for each case in the legend in (a, b).

detector versus zenith angle θ for different GCR spectra under different solar modulations. The results of dose rate per θ angle from GCR protons and ^{4}He ions are shown in panels (a) and (b), respectively.

Figures 6a and 6b show that the surface downward radiation dose of particles depends on the zenith angle, θ. For instance, protons coming in at an angle of about 75° contribute more to the RAD-B dose distribution than protons coming in at other angles. For helium ions, this angle is smaller, about 45°. As described by Guo, Khaksarighiri, et al. (2021), two factors play a role here: (a) the atmospheric column depth increases from about 21 g/cm^2 at $\theta = 0°$ to more than 400 g/cm^2 at the horizon; a thicker traverse path would result in primaries losing more energy and becoming more ionizing or more easily stopped before reaching the surface; moreover, more secondaries are generated along a thicker path and can contribute to the total dose; (b) the area of the source particles incident at each degree of zenith angle is different (distributed as rings on the spherical shell), and it increases with θ. These two concurrent reasons result in the directionality of the dose rate on the surface of Mars as shown in (a) and (b). Scaling the dose by the geometric factor of the ring source using Equation 6, removes the influence of the second factor and one obtains the dose rate in units of [μGy/day/cm^2/sr] as a function of θ as shown in Figures 6c and 6d for protons and helium ions, respectively.

$$\dot{D}\left(\mu Gy/day/cm^2/sr\right) = \left\{\frac{\dot{D}}{\sin(\theta) \times 2\pi \times r^2}\right\}, \tag{6}$$

This normalization accounts for the variation in the area exposed to the radiation and enables comparison of the dose at different points on the surface of the hemisphere. The proton functions in (c) show an almost isotropic profile before gradually increasing to the major peak at $\theta \sim 75°$. This peak arises from the combination of primary protons slowing down and the efficient generation of secondary particles. On the other hand, the induced dose deposit from helium ions decreases monotonically with θ (or the traverse depths) since they have a smaller mean free path and are more likely to fragment in the atmosphere. But at θ between $\sim 10°$ and $\sim 45°$, Helium functions also show an approximately isotropic distribution.

Figure 6 also clearly shows that the surface dose rate depends on solar modulation with smaller modulation potential resulting in a larger dose rate for each θ. With the modulation parameter varying between 800 and 400 MV, the total dose rate in the B detector of RAD varies between 106 and 175 μGy/day for protons, which is about 3.9–4.8 times larger than that induced by helium ions (27–36 μGy/day). The summed proton and helium dose with Φ of 400 MV (solar minimum) is 211 μGy/day in silicon or 281 μGy/day in water. During the deep solar minimum in 2019, the dose rate measured in RAD's silicon detector B is about 230 μGy/day and about 310 μGy/day in its tissue-equivalent detector E (Ehresmann et al., 2022; Guo, Zeitlin, et al., 2021). Our model estimation is about 10% lower than the RAD measurements. Considering that the current model does not include ions heavier than helium ions and also does not include albedo particles (both will be explained in more details later in Section 3.3), the model values reported here are in reasonable agreement with RAD measurements.

3.3. Model Validation: Predictions of the Acceptance Cone Dose Compared With RAD Measurements

The telescope geometry for charged-particle detection in RAD is defined using the A and B detectors as shown in Figure 3. Charged particles entering RAD from the top are measured in a view-cone with an opening half-angle of about 32°. Two view cones are defined by a coincidence of hits in the A and B detectors, which both are 300 μm thick (Hassler et al., 2012). The first cone uses the inner segment, that is, A2 detector, which spans a half angle of 18°, and the other one uses the outer segment, A1 detector, so that the larger cone has a half angle of 32°. As the angular dependence calculated from our model is for each zenith angle shaped as a ring, but the RAD A and B detectors are hexagonal, we assumed that the hexagonal shape can be well approximated by a circular shape and the opening angles reported here are averaged angles, which are <18° half angle and 18°–32° half angle for the A2B and A1B, respectively.

Linear Energy Transfer(LET, dE/dx) is measured in RAD B for an incoming charged particle that satisfies either the A1B coincidence or the A2B coincidence. LET is the amount of ionizing energy that an ionizing particle transfers to the material traversed per unit distance. The unit usually used for this quantity is (keV/μm). LET is an average quantity because, at the microscopic level, the energy per unit length of the track varies over a wide range. The LET of charged particles is a function of particle velocity, β, or kinetic energy, and its charge, Z, and is approximately proportional to Z^2/β^2 (Bethe, 1930; Bloch, 1933; Grimes et al., 2017). This measured quantity is referred to hereinafter as the "LET dose," since we use that term below. RAD records the energy deposited in B within the LET view cone for every particle without determining Z and β of each particle. As a result, the energy distribution contributed by all particles entering the cone and penetrating through B is recorded as an onboard histogram and sent back to Earth (Hassler et al., 2012). This histogram of energy deposits can be used to derive the LET or dE/dx histogram using the mean path length, dx, of particles inside the A1B or A2B cone.

We sum over all the onboard dE histograms to derive the total absorbed energy in silicon detector B from particles coming through the acceptance cone.

RAD is mounted in the Curiosity rover with its central axis perpendicular to the rover deck, and its fields of view are centered vertically when the rover is on flat ground, that is, the center of the acceptance cone would correspond to $\theta = 0°$ when the rover is horizontal. However, along the traverse of Curiosity, the rover body was generally not exactly horizontal, as it would be on level ground. Guo, Zeitlin, et al. (2021, Figure 16) shows the zenith tilt angle of the rover body through the first 2800 sols after MSL landed on Mars. The rover is tilted at angles up to about 25° from the zenith, with an average value of 7.3°. If we expect the downward radiation to be nonisotropic within the tilt angles experienced by Curiosity, we would observe a change of the LET-dose as the rover changes its inclination, for example, when ascending a slope.
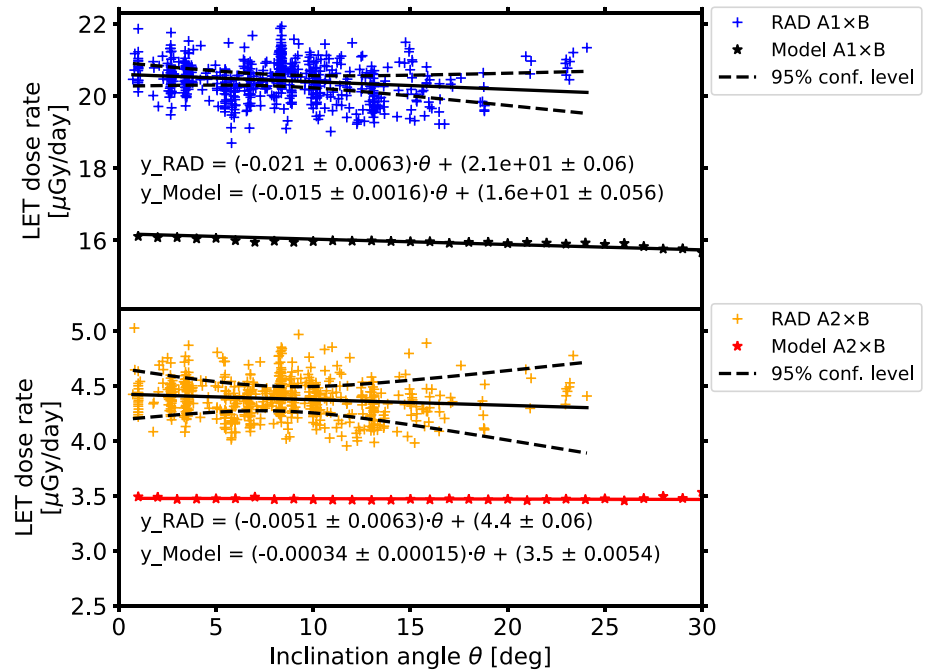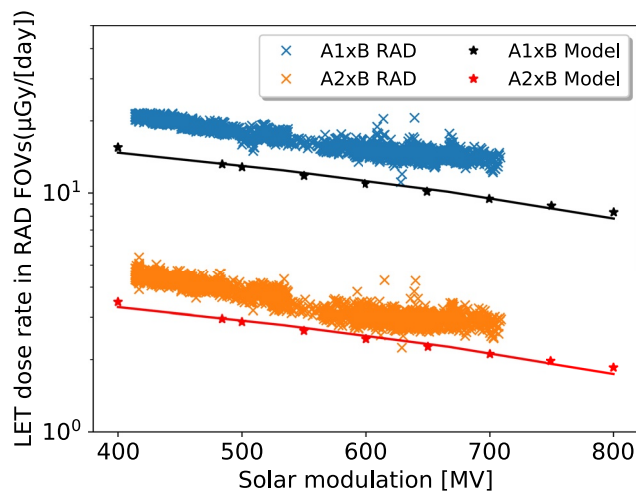
Figure 7. LET dose rate within the inner view cones (A2B) and outer cone (A1B) of Radiation Assessment Detector (RAD) derived from the measurements and model predictions versus inclination of RAD.

In the following, we will compare the dose rates integrated from the LET spectra with the model predictions presented in Section 3.2. As our model contains the θ-dependent dose, it is straightforward to derive the total dose integrated within the acceptance cone given the viewing angle of the cone and the inclination of the rover (the inclination angle equals the zenith angle of the central axis of the cone). Because of the hexagonal shape of the individual RAD detector segments, this calculation cannot be performed analytically but is best calculated numerically. To do so, we first calculate the function for the proportion of the source ring area inside the RAD's field of view cones (half opening angles of 18° (A2B) and 32°(A1B)) and then multiplied these functions with our dose functions shown in Figures 6a and 6b.

Next, we investigate whether the observed or modeled LET dose depends on the rover inclination angle. To do so, we need to minimize the influence of other factors on the Martian surface radiation (Guo, Zeitlin, et al., 2021). The most pronounced one is the solar modulation which drives the long-term variations of the GCR radiation on Mars. Here, we select the data with monthly Φ between 420 and 430 MV as derived by the Oulu Neutron Monitor (https://cosmicrays.oulu.fi) to minimize the impact of solar modulation. Note that modulation factors could be different between Earth and Mars (Guo et al., 2015). However, as a statistical study integrated through a long time period, we do not expect this difference to significantly impact our results because the modulation is equal *on average*—except for a very weak radial dependence (Saganti, 2005).

Figure 7 shows LET-derived dose rates for the view cones spanned by RAD's A1-B and A2-B detectors. The acceptance cone dose from the RAD measurement and the derived data from the model in different view cones, which were selected under a specific modulation for the inclination angle covered by RAD as shown in this figure. As one can see, the data are consistent with no slope at the 95% confidence level. The measurements cover inclination angles up to ~24° while the model prediction extends to larger values. It shows that the LET dose does not depend on the inclination angle within the range of 60°. This is related to the fact that both proton and helium doses are not far from isotropic for θ below ~50° and also that the acceptance cone is perhaps too large to detect the change of the fields. This result is consistent with that obtained by Wimmer-Schweingruber et al. (2015) over a narrower range of rover tilt angles. The variations in Figure 7 in RAD data are due to changes in pressure, the range in solar modulation that is included in the RAD data, and other small perturbations, which affect the measurements (Guo, Zeitlin, et al., 2021).

However, there is a difference of about 28% between the RAD measurement and our model for both A1B and A2B cones. There are two reasons for this difference. First, we only considered protons and ^{4}He ions as primary

Figure 8. LET dose rate within the two view cones of Radiation Assessment Detector derived from the measurement and modeling data versus the solar modulation parameter Φ. The difference between the modeled results and the measurement is expected, as explained in the main text.

GCRs in our model, but other species of GCR ions with high (H) atomic number (Z) and energy (E) (HZE ions) also contribute to the dose deposit in RAD data. Primary GCRs heavier than protons and helium ions contribute around 10% to the total absorbed dose on the surface of Mars as suggested by results of simulations including both light and heavy ions (Zhang et al., 2022, Figure 7). But the 28% difference reported here is significantly larger than the expected 10% contribution by HZE particles. Moreover, it is also higher than the 10% difference when considering the modeled and measured dose integrated over all zenith angles as discussed in the previous section. The most likely explanation is that the contribution from HZEs is higher since the average path length through the Martian atmosphere is shorter, resulting in less fragmentation of heavy ions before reaching RAD than within the acceptance cone as compared to directions outside the cone.

Second, secondary particles created in the Martian soil (so-called albedo particles which move upward, away from Mars) also in principle contribute to the measured LET-cone dose rate. Guo, Khaksarighiri, et al. (2021) used the absorbed dose in the plastic detector "E" and estimated that the albedo radiation, measured as an absorbed dose by RAD, on flat terrain is about 19% of the total surface dose. Although these albedo particles need energy higher than about 110 MeV/nuc to reach the B detector, and the low-energy albedo particles traveling upward from the surface are likely to deposit energy in E and stop in the detector stack before reaching B. But, they can contribute slightly to the dose in the B detector (Appel et al., 2018). Considering both the HZE and albedo contributions to the LET dose, the 28% difference between our model and the RAD measurement is rather reasonable.

Finally, we consider the influence of solar modulation on the Martian surface radiation. This has been quantified as the most important factor that affects the long-term dose rate recorded by MSL/RAD (Guo, Zeitlin, et al., 2021). As shown in Figure 8, both the RAD-measured LET dose and modeled LET-cone dose are anticorrelated with the solar modulation potential Φ as also shown in previous studies of the RAD GCR radiation dose (Guo, Zeitlin, et al., 2021; Zeitlin et al., 2019). The ~28% difference between the modeled results and measurements has the same origin as that in Figure 7, as discussed before.

4. Summary and Conclusion

We used a Geant4 model to investigate the zenith-angle dependence of the downward radiation field on the surface of Mars and have compared this with measurements obtained with the RAD instrument on the MSL Curiosity rover. We investigated the two largest contributions to the surface dose: energetic protons and helium nuclei. The latter can fragment as they interact with the Martian atmosphere. At sufficiently high energies, both types of particles can lead to cascades of secondary particles, at lower energies, their main interaction is by ionization. The model takes into account the increase in column depth with increasing zenith angle. The calculations were performed for a model spectrum with a power-law index of −1 and stored as Mars atmosphere "response functions." These were subsequently folded with the Badhwar-O'Neill (O'Neill et al., 2015) GCR model spectra for a representative range of solar modulation potentials.

The model results suggest that the radiation dose is nonisotropic on the surface of Mars, especially at large zenith angles >60°. We cannot exclude an isotropic behavior at the 95% confidence level within the ~25° range of inclination angles experienced by Curiosity in the course of its mission on Mars. This is consistent with and extends a previous study by Wimmer-Schweingruber et al. (2015), which, however, did not cover a wide range of inclination angles.

We found that the RAD measurements show an average dose rate that is about 28% higher than our model results. However, when considering the full sky view, that is, integrating over all zenith angles, this difference is only about 10% as explained in Section 3.2. Moreover, previous model results show that HZE ions contribute about 10% to the total dose on the surface of Mars (Röstel et al., 2020; Zhang et al., 2022) when considering particles arriving from the full sky view. We expect that this discrepancy between 28% and 10% is due to the fragmentation

of HZE particles at large zenith angles because such particles need to traverse a significantly larger column depth. Because the Geant4 calculations for such particles are extremely time consuming, we have not yet been able to perform them and will report them in a forthcoming publication.

As is well-known, HZE ions may contribute significantly to cell damage because the energy deposited in an individual cell is proportional to the square of the particle's charge. For deep space missions to Mars, GCR HZE ions induced radiation has been a major concern (Cucinotta & Durante, 2006). Our study suggests that the HZE contribution could be higher at smaller zenith angles for explorers on the surface of Mars. This indicates that extra shielding against radiation is particularly important toward the zenith than toward the horizon.

Data Availability Statement

The data used in this study are archived in the NASA Planetary Data System's Planetary Plasma Interactions Node at the University of California, Los Angeles. The archival volume includes the full binary raw data files, detailed descriptions of the structures, and higher level data products in human-readable form. The binary RAD EDR data are archived under (Peterson et al., 2013), while the human-readable RAD RDR data are archived under (Rafkin et al., 2013). The MSL/REMS data archived in the NASA planetary data systems' planetary plasma interactions node (Gomez Elvira, 2013). Data plotted in the figures are available via (Khaksarighiri, 2022). The data are available in txt format and contain the columns with the x- and y-values for the data points plotted in the figures. More information about the structure of the files is contained within the files themselves.

References

Agostinelli, S., Allison, J., Amako, K., Apostolakis, J., Araujo, H., Arce, P., et al. (2003). GEANT4: A simulation toolkit. *Nuclear Instruments & Methods*, *A506*(3), 250–303. https://doi.org/10.1016/S0168-9002(03)01368-8

Allison, J., Amako, K., Apostolakis, J., Araujo, H., Arce Dubois, P., Asai, M., et al. (2006). GEANT4 developments and applications. *IEEE Transactions on Nuclear Science*, *53*(1), 270–278. https://doi.org/10.1109/TNS.2006.869826

Allison, J., Amako, K., Apostolakis, J., Arce, P., Asai, M., Aso, T., et al. (2016). Recent developments in GEANT4. *Nuclear Instruments & Methods A*, *835*, 186–225. https://doi.org/10.1016/j.nima.2016.06.125

Appel, J., Köehler, J., Guo, J., Ehresmann, B., Zeitlin, C., Matthiä, D., et al. (2018). Detecting upward directed charged particle fluxes in the Mars Science Laboratory radiation assessment detector. *Earth and Space Science*, *5*(1), 2–18. https://doi.org/10.1002/2016EA000240

Barcellos-Hoff, M. H., Blakely, E. A., Burma, S. E., Fornace, A. J., Gerson, S., Hlatky, L., et al. (2015). Concepts and challenges in cancer risk prediction for the space radiation environment. *Life Sciences and Space Research*, *6*, 92–103. https://doi.org/10.1016/j.lssr.2015.07.006

Bethe, H. (1930). Zur Theorie des Durchgangs schneller Korpuskularstrahlen durch Materie. *Annalen der Physik*, *397*(3), 325–400. https://doi.org/10.1002/andp.19303970303

Bloch, F. (1933). Bremsvermögen von Atomen mit mehreren Elektronen. *Zeitschrift fur Physik*, *81*(5–6), 363–376. https://doi.org/10.1007/BF01344553

Cucinotta, F. A., Alp, M., Sulzman, F. M., & Wang, M. (2014). Space radiation risks to the central nervous system. *Life Sciences and Space Research*, *2*, 54–69. https://doi.org/10.1016/j.lssr.2014.06.003

Cucinotta, F. A., & Durante, M. (2006). Cancer risk from exposure to galactic cosmic rays: Implications for space exploration by human beings. *The Lancet Oncology*, *7*(431–436), 682–688. https://doi.org/10.1016/S1470-2045(06)70695-7

Ehresmann, B., Zeitlin, C., Hassler, D., Guo, J., Wimmer-Schweingruber, R., Berger, T., et al. (2022). The Martian surface radiation environment at solar minimum measured with MSL/RAD. *Icarus*, *393*, 115035. https://doi.org/10.1016/j.icarus.2022.115035

Gomez Elvira, J. (2013). MSL rover environmental monitoring station RDR data V1.0, MSL-M-REMS-4-ENVEDR-V1.0. *NASA Planetary Data System*. https://doi.org/10.17189/1523028

Gómez-Elvira, J., Armiens, C., Castañer, L., Domínguez, M., Genzer, M., Gómez, F., et al. (2012). REMS: The environmental sensor suite for the Mars Science Laboratory rover. *Space Science Reviews*, *170*(1–4), 583–640. https://doi.org/10.1007/s11214-012-9921-1

Grimes, D. R., Warren, D. R., & Partridge, M. (2017). An approximate analytical solution of the bethe equation for charged particles in the radiotherapeutic energy range. *Scientific Reports*, *7*(1), 1–12. https://doi.org/10.1038/s41598-017-10554-0

Guo, J., Banjac, S., Röstel, L., Terasa, J. C., Herbst, K., Heber, B., & Wimmer-Schweingruber, R. F. (2019). Implementation and validation of the GEANT4/AtRIS code to model the radiation environment at Mars. *Journal of Space Weather and Space Climate*, *9*(A2), A2. https://doi.org/10.1051/swsc/2018051

Guo, J., Khaksarighiri, S., Wimmer-Schweingruber, R. F., Hassler, D. M., Ehresmann, B., Zeitlin, C., et al. (2021). Directionality of the Martian surface radiation and derivation of the upward albedo radiation. *Geophysical Research Letters*, *48*(15), e2021GL093912. https://doi.org/10.1029/2021GL093912

Guo, J., Slaba, T. C., Zeitlin, C., Wimmer-Schweingruber, R. F., Badavi, F. F., Böhm, E., et al. (2017). Dependence of the Martian radiation environment on atmospheric depth: Modelling and measurement. *Journal of Geophysical Research: Planetary Science*, *122*(2), 329–341. https://doi.org/10.1002/2016je005206

Guo, J., Zeitlin, C., Wimmer-Schweingruber, R. F., Rafkin, S., Hassler, D. M., Posner, A., et al. (2015). Modeling the variations of dose rate measured by RAD during the first MSL Martian year: 2012–2014. *The Astrophysical Journal*, *810*(1), 24. https://doi.org/10.1088/0004-637X/810/1/24

Guo, J., Zeitlin, R. F., Wimmer-Schweingruber, C., Hassler, D. M., Ehresmann, B., Rafkin, S., et al. (2021). Radiation environment for future human exploration on the surface of Mars: The current understanding based on MSL/RAD dose measurements. *Astronomy and Astrophysics Review*, *29*(1), 1–81. https://doi.org/10.1007/s00159-021-00136-5

Hassler, D. M., Zeitlin, C., Wimmer-Schweingruber, R., Böttcher, S., Martin, C., Andrews, J., et al. (2012). The radiation assessment detector (RAD) investigation. *Space Science Reviews*, *170*(1–4), 503–558. https://doi.org/10.1007/s11214-012-9913-1

Kennedy, A. R. (2014). Biological effects of space radiation and development of effective countermeasures. *Life Sciences and Space Research*, *1*, 10–43. https://doi.org/10.1016/j.lssr.2014.02.004

Khaksarighiri, S. (2022). Data to reproduce figures in Khaksarighiri et al. (2023), JGR Planets. [Dataset]. Zenodo. https://doi.org/10.5281/zenodo.7257306

Khaksarighiri, S., Guo, J., Wimmer-Schweingruber, R., & Narici, L. (2021). An easy-to-use function to assess deep space radiation in human brains. *Scientific Reports*, *11*(1), 1–12. https://doi.org/10.1038/s41598-021-90695-5

Matthiä, D., Ehresmann, B., Lohf, H., Köhler, J., Zeitlin, C., Appel, J., et al. (2016). The Martian surface radiation environment–a comparison of models and MSL/RAD measurements. *Journal of Space Weather and Space Climate*, *6*(27), 1–17. https://doi.org/10.1051/swsc/2016008

Millour, E., Forget, F., Spiga, A., Navarro, T., Madeleine, J.-B., Montabone, L., et al. (2015). The Mars climate database (MCD version 5.2). *European planetary science congress*, *10*, 2015–2438.

O'Neill, P., Golge, S., & Slaba, T. (2015). *Badhwar–O'Neill 2014 galactic cosmic ray flux model*. NASA/TP. Retrieved from https://ntrs.nasa.gov/archive/nasa/casi.ntrs.nasa.gov/20150003026.pdf

Peterson, J, Rafkin, S., Zeitlin, C., Ehresmann, B., Weigle, E., Jeffers, S., & Hassler, D. M. o. (2013). MSL Mars radiation assessment detector RDR V1.0, MSL-M-RAD-3-RDR-V1.0. *NASA Planetary Data System*. https://doi.org/10.17189/1519761

Rafkin, S., Peterson, J., Zeitlin, C., Ehresmann, B., Weigle, E., & Hassler, D. M. o. (2013). MSL Mars radiation assessment detector EDR V1.0, MSL-M-RAD-2-EDR-V1.0t. *NASA Planetary Data System*. https://doi.org/10.17189/1519760

Rafkin, S. C., Zeitlin, C., Ehresmann, B., Hassler, D., Guo, J., Köhler, J., et al. (2014). Diurnal variations of energetic particle radiation at the surface of Mars as observed by the Mars Science Laboratory Radiation Assessment Detector. *Journal of Geophysical Research: Planets*, *119*(6), 1345–1358. https://doi.org/10.1002/2013je004525

Röstel, L., Guo, J., Banjac, S., Wimmer-Schweingruber, R. F., & Heber, B. (2020). Subsurface radiation environment of Mars and its implication for shielding protection of future habitats. *Journal of Geophysical Research: Planets*, *125*(3), e2019JE006246. https://doi.org/10.1029/2019JE006246

Saganti, P. (2005). Marie measurements and model predictions of solar modulation of galactic cosmic rays at Mars.

Simpson, J. (1983). Elemental and isotopic composition of the galactic cosmic rays. *Annual Review of Nuclear and Particle Science*, *33*(1), 323–382. https://doi.org/10.1146/annurev.ns.33.120183.001543

Wilson, J., Clowdsley, M., Cucinotta, F., Tripathi, R., Nealy, J., & De Angelis, G. (2004). Deep space environments for human exploration. *Advances in Space Research*, *34*(6), 1281–1287. https://doi.org/10.1016/j.asr.2003.10.052

Wimmer-Schweingruber, R. F., Köhler, J., Hassler, D. M., Guo, J., Appel, J.-K., Zeitlin, C., et al. (2015). On determining the zenith angle dependence of the Martian radiation environment at gale crater altitudes. *Geophysical Research Letters*, *42*(24), 10–557. https://doi.org/10.1002/2015GL066664

Zeitlin, C., Hassler, D., Ehresmann, B., Rafkin, S., Guo, J., Wimmer-Schweingruber, R. F., et al. (2019). Measurements of radiation quality factor on Mars with the Mars Science Laboratory radiation assessment detector. *Life Sciences and Space Research*, *22*, 89–97. https://doi.org/10.1016/j.lssr.2019.07.010

Zhang, J., Guo, J., Dobynde, M. I., Wang, Y., & Wimmer-Schweingruber, R. F. (2022). From the top of Martian Olympus to deep craters and beneath: Mars radiation environment under different atmospheric and regolith depths. *Journal of Geophysical Research: Planets*, *127*(3), e2021JE007157. https://doi.org/10.1029/2021je007157